
This manuscript is a preprint and has been submitted for publication in **Journal of Glaciology**. It has been revised after peer review but **not yet accepted for publication**. Subsequent versions of this manuscript may differ due to the editorial process. If accepted for publication, the final version will be available via the "Peer-reviewed publication DOI" link on EarthArXiv. We hope you find this paper interesting and would welcome your feedback on it. Please contact Mike Prior-Jones or Liz Bagshaw with your feedback using the email addresses on the following page.

1 Cryoegg: development and field trials of a wireless subglacial probe for deep, fast-moving ice

2 Michael Prior-Jones¹, Elizabeth A. Bagshaw¹, Jonathan Lees², Lindsay Clare³, Stephen Burrow³, Mauro
3 A Werder⁴, Nanna B. Karlsson⁵, Dorthe Dahl-Jensen^{6,7}, Thomas R. Chudley⁸, Poul Christoffersen⁸,
4 Jemma Wadham⁹, Samuel H Doyle¹⁰, Bryn Hubbard¹⁰

5 ¹School of Earth and Ocean Sciences, Cardiff University, Cardiff, UK (prior-jonesm@cardiff.ac.uk;
6 bagshawe@cardiff.ac.uk)

7 ²School of Engineering, Cardiff University, Cardiff, UK

8 ³Department of Aerospace Engineering, University of Bristol, Bristol, UK

9 ⁴Laboratory of Hydraulics, Hydrology and Glaciology, ETH Zürich, Zürich, Switzerland

10 ⁵Geological Survey of Denmark and Greenland, Copenhagen, Denmark

11 ⁶Niels Bohr Institute, University of Copenhagen, Copenhagen, Denmark

12 ⁷Center for Earth Observation Science, University of Manitoba, Winnipeg, Canada

13 ⁸Scott Polar Research Institute, University of Cambridge, Cambridge, UK

14 ⁹School of Geographical Sciences, University of Bristol, Bristol, UK

15 ¹⁰Department of Geography and Earth Sciences, Aberystwyth University, Aberystwyth, UK

16 ABSTRACT

17 Subglacial hydrological systems require innovative technological solutions to access and observe.
18 Wireless sensor platforms can be used to collect and return data, but their performance in deep and
19 fast-moving ice requires quantification. We report experimental results from Cryoegg: a spherical
20 probe that can be deployed into a borehole or moulin and transit through the subglacial hydrological
21 system. The probe measures temperature, pressure and electrical conductivity in-situ and returns all
22 data wirelessly via a radio link. We demonstrate Cryoegg's utility in studying englacial channels and
23 moulins, including in-situ salt dilution gauging. Cryoegg uses very high frequency (VHF) radio to
24 transmit data to a surface receiving array. We demonstrate transmission through up to 1.3 km of cold
25 ice - a significant improvement on the previous design. The wireless transmission uses Wireless M-Bus
26 on 169 MHz; we present a simple radio link budget model for its performance in cold ice and
27 experimentally confirm its validity. Cryoegg has also been tested successfully in temperate ice. The
28 battery capacity should allow measurements to be made every two hours for more than a year. Future
29 iterations of the radio system will enable Cryoegg to transmit data through up to 2.5 km of ice.

30 INTRODUCTION

31 The presence and behaviour of liquid water in the subglacial environment governs the response of ice
32 to climate warming. Meltwater generated on the surface makes its way to the bed via networks of
33 moulins, cracks and crevasses (Chu, 2014; Flowers, 2018). Once at the bed, it flows to the ice margins
34 either through a subglacial drainage network consisting of inefficient linked cavities (Iken and
35 Bindschadler, 1986; Walder, 1986; Kamb, 1987), efficient channels carved into rock, ice or the
36 sediment below (Röthlisberger, 1972; Nye, 1976; Clarke, 1987; Ng, 2000), or a combination of both
37 (Hoffman and others, 2016). The configuration of the drainage network determines the subglacial
38 water pressure and how much of the ice-bed interface is in contact with liquid water. Contact
39 promotes sliding (Kamb, 1970; Iken, 1981; Schoof, 2010), which in turn can cause ice to accelerate
40 downstream. In recent years, the relationship between meltwater supply and ice acceleration has
41 been reevaluated in light of observations from the margins of the Greenland Ice Sheet that
42 demonstrate a seasonal evolution of subglacial drainage systems (Chandler and others, 2013;
43 Tedstone and others, 2015) commonly observed in Alpine systems (Nienow and others, 2005). Early
44 in the melt season, an increased flux of meltwater is routed to the bed and the low capacity,
45 inefficiently linked cavity system is forced to expand, forming efficient channels that can transport
46 substantial volumes of water. This reduces the area of the bed in contact with water, and potentially

47 regulates the flow of ice (Sole and others, 2011; Tedstone and others, 2015; Nienow and others, 2017;
48 Flowers, 2018). The defining feature of these different drainage configurations is the water pressure:
49 channelised systems operate at lower pressure than linked cavities, thus measurement of the
50 subglacial water pressure can be used to determine the likely structure of the drainage system, and
51 hence the acceleration response of the ice to increased surface melt inputs.

52 In addition to water pressure, other parameters may provide clues as to the structure of the drainage
53 system, but distinction between drainage system types is challenging. Temperature can be used to
54 assess whether the bed is at the pressure melting point, and the residence time of water in the system
55 can be used, in conjunction with pressure, to assess how efficiently the meltwater transits the system.
56 Long residence times are common in linked cavity systems, which results in prolonged contact
57 between meltwater and subglacial sediment (Tranter and others, 2002). This promotes chemical
58 weathering and changes the composition of the meltwater, so meltwater chemistry is a good indicator
59 of drainage system structure. Chemical composition is challenging to assess in situ, but a
60 measurement of the total dissolved solids can be easily obtained via a measurement of electrical
61 conductivity (Hubbard and others, 1995).

62 These three parameters (pressure (P), temperature (T) and electrical conductivity (EC)) are relatively
63 easy to measure via electronic sensors and can thus be combined to provide information on subglacial
64 drainage that could not be detected from the surface. Measuring these parameters subglacially is,
65 however, extremely challenging, particularly beneath thick, fast flowing ice. Yet it is these fast-flowing
66 sectors that govern the response of large ice masses to climate warming, since they transfer significant
67 volumes of ice to the ocean (Pritchard and others, 2009; van den Broeke and others, 2016). Drilling
68 boreholes through a glacier to access subglacial hydrological channels is logistically demanding and
69 disturbs the system that is under study. Once boreholes are drilled, implanting cabled sensors is
70 possible, but ice motion causes cables to flex and eventually break (Iken and others, 1993; Doyle and
71 others, 2018). In fast-flowing ice, data capture is thus limited to days or weeks. An alternative method
72 is therefore required that can capture these relatively simple electrical measurements and return
73 them to the surface without requiring a physical connection. A wireless radio frequency (RF) system
74 is ideal and there is a long history of the use of RF propagation through ice (see Plewes and Hubbard,
75 2001 for a review).

76 Here, we present trials of Cryoegg, a wireless sensor platform for use in deep ice. The use of a radio
77 link for subglacial telemetry has been proven by the work of the Glacsweb programme (Martinez and
78 others, 2004; Hart and others, 2019) and the WiSe project (Smeets and others, 2012). Previous work
79 (Bagshaw and others, 2014) showed that a 'Cryoegg' concept was feasible, namely a spherical sensor
80 platform containing all sensor, radio and datalogger components that could fit in a standard borehole
81 and travel through subglacial meltwater pathways: the electronics could be made sufficiently
82 compact, and that the radio link worked through up to 500m of ice. However, the radio link design
83 chosen proved unsuitable for performance in very deep ice, so design improvements were required.
84 In this paper we describe the redesign of Cryoegg to give enhanced radio link performance and show
85 the outcomes of field trials at sites in Greenland and the Swiss Alps.

86 In order to measure subglacial hydrological properties in deep polar ice, the enhanced Cryoegg had to
87 meet or exceed the following engineering constraints:

- 88 • An outer diameter of 120 mm or less, to fit into a standard ice core borehole
- 89 • A radio link capable of reaching the surface through 2,500 m of ice, the mean bed depth in
90 central Greenland (Morlighem and others, 2017)
- 91 • Survive and measure water pressure of up to 25 MPa (250 bar, equivalent to a water column
92 of 2,500 m)
- 93 • Measure temperature, typically in the range from -30 to 0 °C
- 94 • Measure EC, typically in the range from 0.002 - 25 mS m⁻¹ (2 - 250 μS cm⁻¹)
- 95 • A battery life capable of sustaining one measurement every 12 hours for a period of one year

96 RADIO LINK DESIGN

97 The success of the instrument depends principally on the performance of the radio link. The 2012
98 design (Bagshaw and others, 2014) used a simple frequency shift keying (FSK) transmitter operating
99 on 151 MHz and demonstrated a maximum range of 500 m in wet ice. To achieve a greater range, we
100 investigated alternative frequencies and transmission schemes. The power of a radio wave
101 propagating in “free space” (e.g. in air or vacuum) reduces according to an inverse square law with
102 distance - known as “geometric attenuation”. When the propagating wave reaches a receiving
103 antenna, the ability of that antenna to extract power from the incoming wave is the “effective
104 aperture”, and this depends upon the wavelength of the incoming wave. Antenna performance is
105 more usually characterised using the antenna gain, which is the ratio of the antenna’s effective
106 aperture in the direction of the main beam to the effective aperture of an “ideal” isotropic antenna
107 that receives signals equally well in all directions.

108 These effects are collectively described by the free space path loss equation, sometimes known as the
109 Friis transmission equation, which describes how a radio link performs in free space. The equation
110 assumes that the antennas are optimally pointed at one another and that their polarisations match,
111 otherwise there are further losses associated with pointing error and polarisation mismatch. The
112 original paper (Friis, 1946) presents the equation in terms of effective aperture, and in linear units.
113 The more commonly used version quoted here is expressed in terms of antenna gain and uses decibel
114 units.

115 Equation (1), adapted from Griffiths (1987, p. 12), is the free space path loss equation in decibel units:

$$116 P_{rx} = P_{tx} + G_{tx} + G_{rx} - 20 \log_{10} \left(\frac{4\pi d}{\lambda} \right) \quad (1)$$

- 117 • P_{rx} is power at the receiver, in dBW (dB relative to 1 watt)
- 118 • P_{tx} is power transmitted by the transmitter, in dBW
- 119 • G_{tx} is the gain of the transmitting antenna, in dBi (dB relative to the performance of an
120 isotropic antenna)
- 121 • G_{rx} is the gain of the receiving antenna, in dBi
- 122 • d is the distance between the transmitting and receiving antennas in metres
- 123 • λ is the wavelength of the transmission.

124 The last term of Equation (1) is known as the “free space path loss” (FSPL) and combines the geometric
125 attenuation due to distance with the apparent wavelength-related attenuation caused by the effective
126 aperture of the antennas. Consequently, the free space path loss equation gives us the rule of thumb

127 that lower frequencies (longer wavelengths) appear to propagate further than higher frequencies.
 128 FSPL over 2500 m ranges from 70 dB at 30 MHz to 99 dB at 868 MHz (Table 1), depending on frequency.
 129 Table 1: Values of free space path loss in dB for several frequencies used by previous subglacial
 130 wireless transmission systems, the industrial standard LoRaWAN and the redesign of Cryoegg (see
 131 results section).

System	WiSe ^a	eTracer ^b , Cryoegg (2012) ^b , Glacsweb (2012 – present) ^c	Glacsweb (2004 – 2006) ^d	LoRaWAN ^e	Cryoegg (2019)
Frequency (MHz)	30	150	433	868	169
Distance (m)					
100	42.0	56.0	65.2	71.2	57.0
500	56.0	70.0	79.2	85.2	71.0
1000	62.0	76.0	85.2	91.2	77.0
1500	65.5	79.5	88.7	94.7	80.5
2000	68.0	82.0	91.2	97.2	83.0
2500	70.0	83.9	93.1	99.2	85.0

132 a) Smeets and others, 2012; b) Bagshaw and others, 2014; c) Hart and others, 2019 d) Martinez and
 133 others, 2004; e) <https://lora-alliance.org/about-lorawan/>

134 FSPL applies to all radio links regardless of the propagating medium. However, where the medium is
 135 lossy the signal is further attenuated by the interaction between the wave and the medium. Ice is one
 136 such lossy medium. Whilst simple models can predict RF attenuation in pure ice, in reality, glacier ice
 137 is heterogeneous, varying in temperature, pore water and impurity content and it contains cracks,
 138 water pockets and debris. Ultra-high frequencies (UHF, 300 MHz–3 GHz) have been effective for
 139 transmission through deep, cold and uniform ice (Lewis and others, 2015), but any presence of water
 140 in this matrix quickly reduces success due to scattering and attenuative losses. The high frequency
 141 (HF, 3-30 MHz) and very high frequency (VHF, 30-300 MHz) bands have good penetration through ice,
 142 with wavelengths longer than typical englacial water bodies encountered along the transmission path
 143 (asserted by Smeets and others, 2012).

144 The attenuation of electromagnetic waves in glacial ice is reported in the study of high-energy
 145 neutrinos (Barwick and others, 2005; Barrella and others, 2011) as *attenuation length* (L_a) in metres.
 146 This is related to *attenuation coefficient* (α) in decibels per metre by Equation (2) (Barrella and others,
 147 2011):

$$148 \quad L_a = \frac{1}{\ln \sqrt{10^{10} \frac{\alpha}{20}}} \quad (2)$$

149 We can rearrange and simplify Equation (2) to convert attenuation length to attenuation coefficient
 150 in dB m⁻¹ (Equation (3)). Some typical values of attenuation length are shown converted to dB per
 151 kilometre in Table 2.

$$152 \quad \alpha = \frac{20}{(\ln 10)L_a} \quad (3)$$

153

154 Table 2: Attenuation length and corresponding attenuation coefficient from 100 to 5000 m

Attenuation length (L_α), metres	Attenuation coefficient (α), dB km ⁻¹
100	86.9
200	43.4
300	29.0
400	21.7
500	17.4
600	14.5
700	12.4
800	10.9
900	9.7
1000	8.7
1500	5.8
2000	4.3
5000	1.7

155

156 Attenuation lengths determined experimentally vary slightly by frequency (Barwick and others, 2005),
 157 with lower frequencies generally having longer attenuation lengths (and hence lower attenuation
 158 coefficients). Mitigating against both free-space and ice-related losses therefore points towards the
 159 use of lower frequencies for radio links within ice. However, low frequencies imply long wavelengths,
 160 which in turn requires physically large antennas, as an efficient antenna needs to be at least ¼ of a
 161 wavelength long. The WiSe system at 30 MHz has a wavelength of 10 metres and used half-wavelength
 162 dipole receiving antennas which were five metres long (Smeets and others, 2012). Large antennas
 163 become impractical to work with in the field, and we had the additional challenge of needing to fit our
 164 transmitting antenna into the 120 mm diameter Cryoegg enclosure. Our previous work used 151 MHz
 165 (wavelength 2 m), which had given satisfactory performance and allowed the receiving antenna to be
 166 easily carried in the field. The very small size of the Cryoegg enclosure meant that there was limited
 167 value in going to higher frequencies as the benefits of having a better-matched transmitting antenna
 168 were far outweighed by the additional free-space and ice-related losses. We therefore looked for a
 169 system that could operate in the VHF band (30-300 MHz).

170 For frequencies in the VHF range (30-300 MHz) the attenuation lengths reported (Barwick and others,
 171 2005; Barrella and others, 2011) range from 200 m to 3000 m. We take the worst-case figure of 200
 172 m (43.4 dB km⁻¹) as our design criterion for working in warm, wet ice and 400 m (21.7dB km⁻¹) as a
 173 conservative estimate for cold, dry ice (Table 2).

174

175 **METHODS**

176 **Choice of transmission scheme**

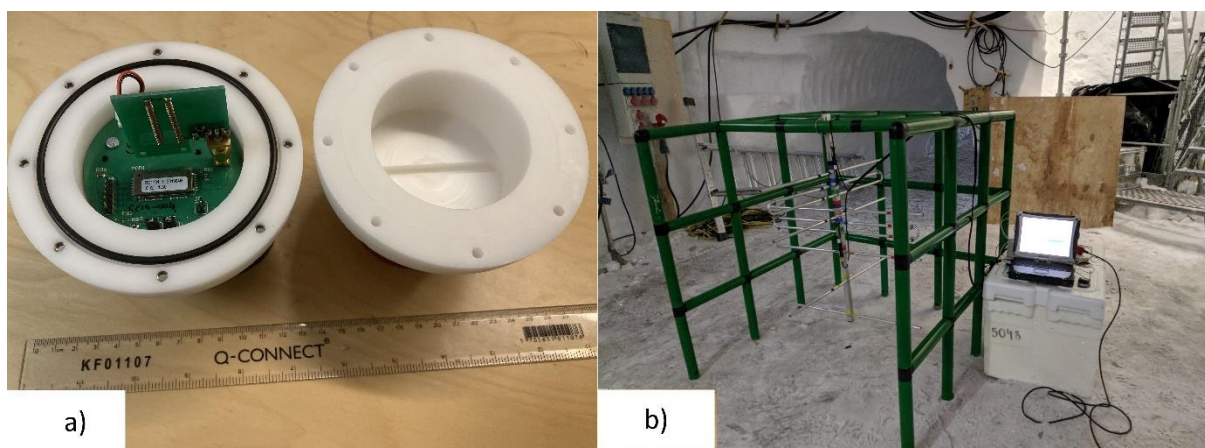
177 The term “transmission scheme” encompasses all the technical aspects of the radio link – the
178 modulation, error corrective coding, packetisation, and higher-level protocols. We required a
179 commercially available system designed for long battery life and for sending small amounts of data
180 over long distances, often sold as low power wide area networks (LPWAN) or “internet of things” (IoT)
181 systems. We selected Wireless M-Bus mode N1 (European Committee for Standardisation, 2013),
182 which is intended for use in utility metering. It is designed to offer very long battery life and sends
183 data at 2.4 kbit s⁻¹. It incorporates error corrective coding, which ensures that data received over the
184 link does not contain errors introduced in transit, and has optional cryptographic protection for
185 security. It operates on the 169 MHz frequency band, which is available for general license-free use in
186 Europe (CEPT ECC Recommendation 70-03). Wireless M-Bus is an open standard and a number of
187 manufacturers provide implementations of it. This gives confidence that the technology will remain
188 available, whereas a proprietary system carries a risk of the product being discontinued.

189 The Radiocrafts RC1701HP-MBUS4 modem used provides 0.5 W (27 dBm) power output on the 169
190 MHz band. One module is fitted to the printed circuit board (PCB) inside Cryoegg, configured as a
191 transmitter. For the receiver, we use Radiocrafts RC1701HP-MBUS4 demo kit with one board
192 configured as a receiver. This board connects to a PC and outputs the decoded data received over the
193 radio link. A Python script running on the PC applies a timestamp to the received packet data and
194 records it in a log file. This approach avoids the need to have a source of accurate time on board
195 Cryoegg.

196 **Antenna selection**

197 The transmitting antenna inside Cryoegg is constrained by the physical size of the spherical case. We
198 chose the HA.10 from Taoglas which is designed for the 169 MHz band, consisting of a pair of 30mm
199 long air-cored helical elements and a matching network. To minimise use of conductive materials
200 around the antenna, the upper hemisphere is devoted to the antenna and the remaining electronics
201 fit into the lower hemisphere (Fig. 1a).

202



203

204 Fig. 1 – a) Cryoegg with upper casework removed b) receiving antenna mounted on plastic frame

205 The receiving antenna on the surface provides additional gain to the system to help overcome the
206 attenuation through the ice, and to compensate for the small size of the transmitting antenna – an
207 ideal antenna would be 450 mm long, yet Cryoegg’s diameter is only 120 mm. We elected to use a

208 pair of crossed Yagi-Uda antennas (Innovantennas), which provide a gain of around 8 dB individually.
209 They are combined through a 90° hybrid combiner (Mini-Circuits part number ZMSCQ-2-180BR+)
210 which makes them behave as a single circularly polarised antenna, but at the expense of 3dB loss in
211 the combiner. By transmitting with linear polarisation and receiving with circular polarisation, we
212 make the radio link performance relatively independent of Cryoegg's orientation. This technique was
213 also used by the WiSe project team (Smeets and others, 2012).

214 The receiving antenna is one metre long. In order to minimise disturbance to the antenna pattern
215 caused by metal parts close to the antenna elements, we used a modular plastic frame (Quadro) to
216 support the antenna (Fig. 1b).

217 The radiation pattern of Cryoegg was assessed in a screened RF test chamber (at the Wolfson Centre
218 for Magnetics in Cardiff) lined with absorbent ferrite material to prevent multipath. A log-periodic
219 antenna was used to receive the signal and the signal level was observed using a spectrum analyser in
220 peak hold mode.

221 Link budget

222 A link budget is used to evaluate whether an attenuation-limited radio link will work in practice.
223 Starting with the power output of the transmitter, gains and losses in the system are totalled up and
224 compared to the sensitivity of the receiver. To allow some margin for unexpected attenuation, we aim
225 for a received power level several dB higher than the sensitivity. Link budgets are traditionally
226 calculated in decibel units as this allows the gains and losses to be added and subtracted (rather than
227 multiplied and divided). Hence we use decibel units of power, such as dBW: decibels relative to one
228 watt, (0 dBW = 1W) or dBm: decibels relative to one milliwatt (0 dBm = 1mW = -30 dBW, and +30 dBm
229 = 1 W = 0 dBW).

230 The link budget calculation (Table 3) assumes a 2000 m borehole through cold ice, with the
231 attenuation coefficient estimated at 21 dB km⁻¹. The performance of the transmit antenna was
232 relatively poor, and so we estimated its gain at -15 dBi (dB relative to an isotropic antenna) based on
233 data from the manufacturer. For the 2000 m example shown here, the received signal margin is 10.5
234 dB.

235

236 Table 3: Link budget calculation for Cryoegg in 2000 m borehole in cold ice (gains are positive values,
 237 losses are negative).
 238

			Link budget contribution	Units
Transmitter power	0.5	W	27.0	dBm
Coupling loss			-0.5	dB
Transmit antenna gain			-15.0	dB
Distance to receiver	2	km		
Frequency	169	MHz		
FSPL			-83.0	dB
Attenuation coefficient for cold ice	21	dB/km		
Ice related loss			-42.0	dB
Crosspolarisation loss			-3.0	dB
Receive antenna gain			8.0	dB
Total power at receiver			-108.5	dBm
Receiver sensitivity	-119	dBm		
Margin			10.5	dB

239 **Sensors**

240 The Keller PA-20D pressure sensor (max. 250 bar) has a vacuum-sealed membrane and communicates
 241 with the microcontroller via the digital I²C interface (Inter-Integrated Circuit; (UM10204 I2C-bus
 242 specification and user manual, 2014)). It provides internal temperature compensation, and supplies a
 243 temperature reading alongside the pressure reading, although the manufacturer does not guarantee
 244 its performance at temperatures below 0 °C. Hence we provided our own independent temperature
 245 sensor (details below). The sensor provides a 16-bit pressure reading to the microcontroller but uses
 246 only half the available range (the rest being used to allow it to report pressures slightly beyond the
 247 calibrated range). This means that the smallest pressure step reportable is 7.6 millibars. The nominal
 248 total error band is 1% of full scale, i.e. 2.5 bar, but in practice we found we could reliably record
 249 changes in water pressure down to 0.1 bar (1m hydrostatic pressure) during field experiments.

250 The temperature and EC sensors are adapted from earlier designs (Bagshaw and others, 2012, 2014).
 251 The EC sensor consists of a square wave oscillator which supplies a 500 kHz waveform to a potential
 252 divider consisting of a precision resistor and a pair of sense electrodes. The sense electrodes are a pair
 253 of M3 stainless steel hex-headed bolts that protrude through the case. The AC waveform from the
 254 midpoint of the potential divider passes through a precision rectifier and RC filter to produce a DC
 255 voltage that varies inversely with EC between the sense electrodes. This is sampled by the
 256 microcontroller’s analogue-to-digital converter (ADC) and the resulting digital value is reported over
 257 the radio link. The temperature sensor is a Pt1000 platinum resistance device, used in a full-bridge
 258 configuration with three fixed resistors. It is driven by a current source and measured using an
 259 instrumentation amplifier, with the output fed to the microcontroller’s ADC. Cryoegg reports the
 260 digital value from the ADC over the radio link, allowing calibration to be carried out externally. The
 261 Pt1000 resistor is mounted to the back of one of the EC sense electrodes with a thermal pad, ensuring
 262 that it has thermal but not electrical contact.

263 **Microcontroller selection**

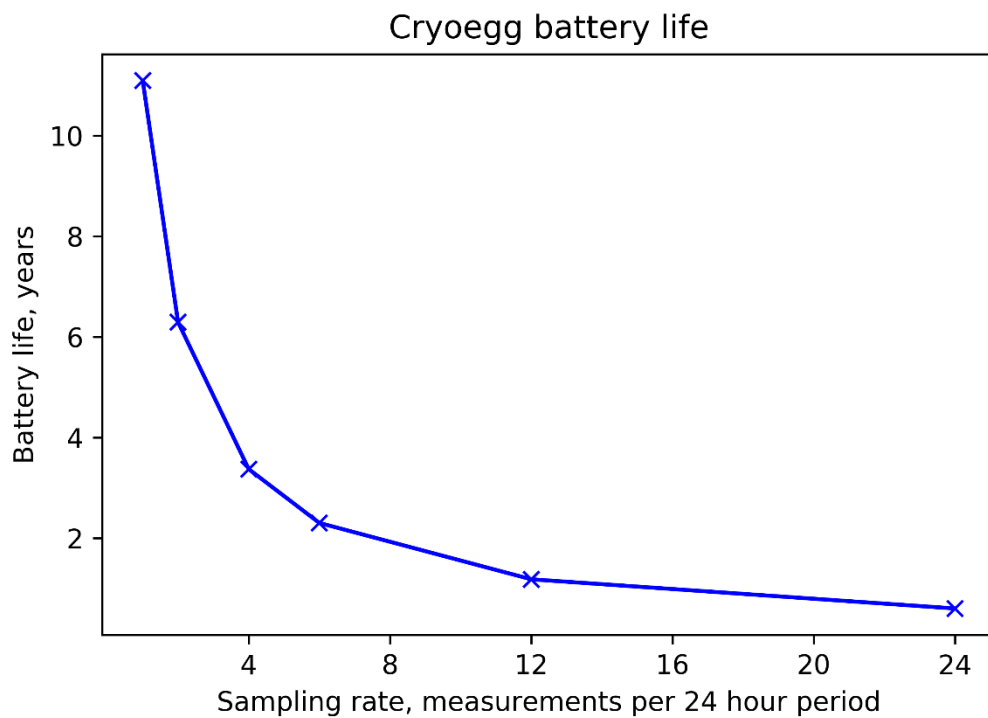
264 To maximise battery life, Cryoegg has a “sleep” mode where most subsystems were powered down
265 between measurements. The STM32L433RCT6P microcontroller (STMicroelectronics) has a built-in
266 Real Time Clock module (RTC) which uses an external quartz crystal oscillator to provide reliable
267 timekeeping at very low power. This “wakes” the microcontroller when it is time for the next
268 measurement. The RTC draws around 500 nA at 3.3 V with the rest of the microcontroller shut down.
269 The microcontroller has a 32-bit ARM Cortex M4 processor that can be clocked at up to 80 MHz, 256
270 kB of flash memory and 64 kB of RAM, and includes the ADC for the temperature and EC sensors; I²C
271 interface for the pressure sensor; and Universal Asynchronous Receiver/Transmitter (UART) for
272 communicating with the radio module. It also controls several power switches that enable and disable
273 power to other parts of the circuit.

274 **Power supply design and power consumption**

275 The radio modem module has relatively high power consumption during transmit – requiring 500 mA
276 at 3.3 V for less than 500 ms during each transmission, which puts a lot of demand on the battery and
277 power supply to be able to supply this peak current. A lithium-polymer rechargeable pouch cell can
278 supply sufficient peak current and be recharged between tests. The battery selected has a 3.7 V
279 nominal voltage and a capacity of 400 mAh.

280 A regulator IC with an enable input (ON Semiconductor NCP115ASN330T2G) supplies 3.3 V to the
281 sensors when enabled, and also provides the ADC reference voltage to the microcontroller. Other
282 parts of the circuit are supplied with unregulated battery voltage.

283 To estimate the battery life, we measured the power consumption of Cryoegg during transmission and
284 during sleep mode in the lab, using a logging multimeter (Mooshim Engineering Mooshimeter) that
285 could measure voltage and current from the battery simultaneously. The measure-and-transmit cycle
286 takes 3.2 seconds and consumes 0.5 J. The sleep mode current consumption proved to be too low for
287 the meter to measure (the lowest current it can record is 5 μ A). We therefore assume that the sleep
288 mode current consumption is that of the microcontroller only (since everything else is disabled) and
289 take the value quoted in the microcontroller datasheet of 500 nA.



290

291 Fig. 2 - Cryoegg projected battery life with varying sampling rate

292

293 The projected battery life based on these measurements is over 6 years at two measurements per
 294 day. Even allowing for some self-discharge in the battery, this gives scope to increase the
 295 measurement frequency. A measurement every 2 hours (i.e. 12 times per day) gives a battery life of
 296 just over a year. Battery life estimates at different sampling rates are shown in Fig. 2. Table A1 in
 297 Appendix A shows an example battery life calculation in more detail.

298 Mechanical design

299 We aimed to provide a simple and robust mechanical design that was straightforward to assemble for
 300 testing. The spherical casework is machined in two halves from acetal copolymer, a hard engineering
 301 plastic (Fig. 1a). The sensor PCB sits directly onto the bottom of the cylindrical internal void and is
 302 secured in place by two M3 threaded spacers, then potted with Raytech Liquid Rubber. There are two
 303 further PCBs that mount above the sensor PCB, which interconnect using multiway connectors. The
 304 processor PCB contains the microcontroller and associated components, and also provides mechanical
 305 support for the battery. The radio PCB is uppermost and supports the radio module, antenna
 306 connector, battery connector and headers for programming and debugging. The pouch cell battery is
 307 sandwiched in the gap between the radio and processor PCBs. The antenna PCB connects to the radio
 308 PCB via an SMA connector and is supported by a groove in the crown of the upper hemisphere. This
 309 design allows the upper hemisphere to be easily removed for access to the electronics, and to connect
 310 the battery before deployment. The upper and lower hemisphere seal with a rubber O-ring and are
 311 held in place by eight machine screws.

312

313 **Software**

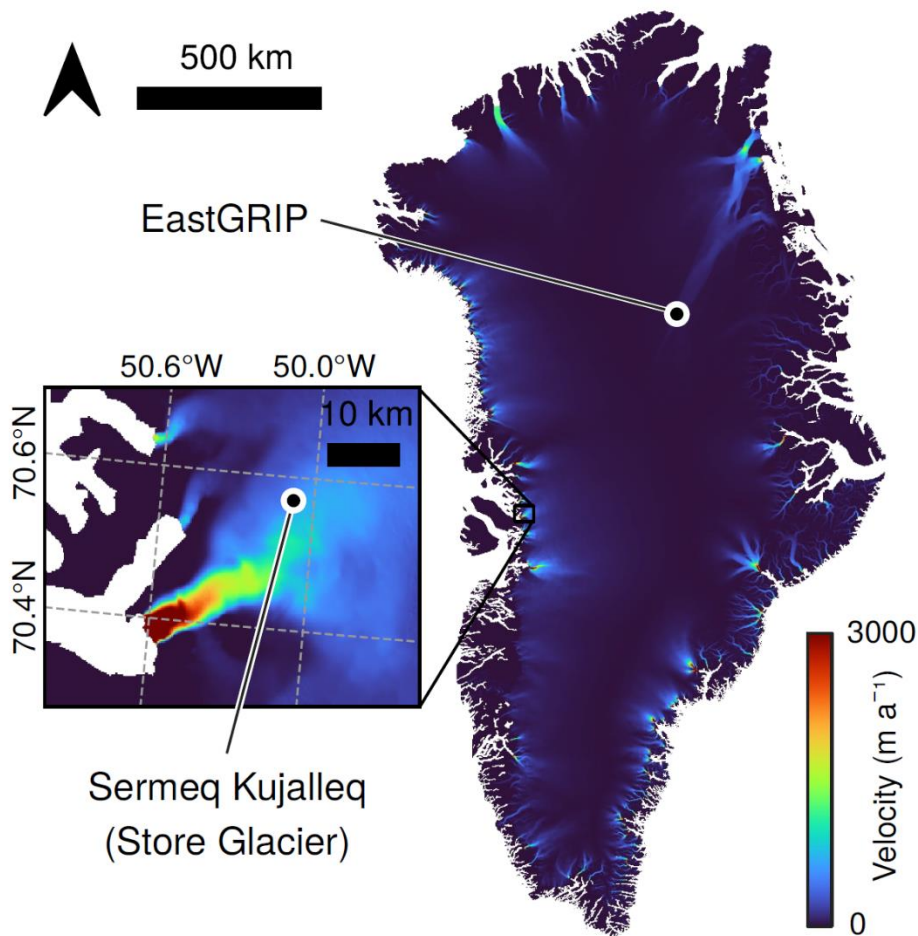
314 The software on the Cryoegg microcontroller is written in C, using the STM32 Hardware Abstraction
315 Libraries. The software goes through the following steps:

- 316 • Power up the sensors
- 317 • Make measurements
- 318 • Power down the sensors
- 319 • Power up the radio module
- 320 • Pack the sensor data into a data packet
- 321 • Send the data packet to the radio module to be transmitted
- 322 • Power down the radio module
- 323 • Set the sleep timer for the next measurement
- 324 • Enter deep sleep (“SHUTDOWN”) mode

325 On awakening from SHUTDOWN mode, the program restarts from the beginning, thus giving an
326 endless loop. The measurements are transmitted immediately after being made, and no data is stored
327 on Cryoegg, since we do not expect to retrieve Cryoegg after deployment.

328 **Field testing**

329 We conducted three field tests during July and August 2019 at two sites in Greenland (EastGRIP drill
330 site and Sermeq Kujalleq/Store Glacier) and one in Switzerland (Rhône Glacier). The objectives of the
331 field tests were to verify the operation of Cryoegg and its receiver in a real glacial environment. We
332 wanted to demonstrate the operation of the radio link in both cold deep ice and shallower temperate
333 ice, and confirm the mechanical integrity of the device when subjected to hydrostatic pressure in fluid-
334 filled boreholes.



335 Fig. 3 - Velocity map of Greenland ice sheet flow, showing locations of EastGRIP and Sermeq Kujalleq
 336 (Store Glacier) test sites in fast flowing ice. Data from MEaSURES dataset of annual Greenland
 337 velocity for 2018 (Joughin and others, 2010; Joughin, 2017).

338 *East Greenland Ice Core Project site (EastGRIP)*

339 EastGRIP is located at N75° 38.05' W036° 00.22' on the North East Greenland Ice Stream (NEGIS), the
 340 largest ice stream in Greenland, which drains 340,000 km^2 of the ice sheet and extends for over 1000
 341 km inland (Fig. 3). Approximately 150 km from the onset, it reaches speeds of 65 m a^{-1} (Joughin and
 342 others, 2010; Karlsson and Dahl-Jensen, 2015). The East Greenland Ice core Project (EastGRIP) is a
 343 unique project drilling an ice core into 2.5 km of fast flowing ice to investigate ice stream beds
 344 (www.eastgrip.org). In summer 2019, the core had been drilled to 2 km depth, leaving behind a 2 km
 345 borehole filled almost completely with drill fluid. The purpose of our field trial at this site was to obtain
 346 a range test for the radio link and a pressure test for the mechanical design. Cryoegg was deployed in
 347 a mesh bag and attached to the main winch (Fig. 4). The orientation of Cryoegg within the bag was
 348 not fully controlled due to its spherical shape, although the pressure sensor protruding through the
 349 mesh helped to prevent it from shifting. The receiving antenna was set up in the drill trench, close to
 350 the winch (Fig. 1b). Cryoegg was lowered and raised into the borehole several times and the received
 351 signal strength (RSSI) and live data stream monitored at the surface, adjacent to the top of the
 352 borehole.



353

354 Fig. 4 – Cryoegg ready for deployment on the EastGRIP ice core winch.

355

356 *RESPONDER site at Sermeq Kujalleq (Store Glacier)*

357 We tested Cryoegg at an inland site (N70° 33.889' W50° 04.558') at Sermeq Kujalleq (Store Glacier),
358 the third fastest outlet glacier in West Greenland (Fig. 3). It has a catchment of 35,000 km² that
359 includes supraglacial lakes that periodically drain via cracks and moulins, several on an annual basis
360 (Chudley and others, 2019). The glacier experiences changes in ice flow associated with sudden
361 injections of meltwater to the pressurised drainage system (Doyle and others, 2018), but the link
362 between surface lake drainage and the subglacial hydrology is poorly defined, primarily because
363 instrumenting a draining lake with cabled sensors is near-impossible. There is extensive supporting
364 data available on the subglacial bed structure, lake drainage frequency and ice strain rates (Hofstede
365 and others, 2018; Young and others, 2018; Chudley and others, 2019). Sermeq Kujalleq (Store Glacier)
366 is the site of the RESPONDER project (“Resolving Subglacial Properties, hydrological networks and
367 dynamic evolution of ice flow on the Greenland Ice Sheet”, <https://www.erc-responder.eu/>), offering
368 access to the glacier bed through hot water drilling. The ice is approximately 1 km thick at this site
369 (Morlighem and others, 2017) and moving at 600 m a⁻¹ (Chudley and others, 2019). Bed access holes
370 were hot water drilled in July 2019.

371 A surface propagation test assessed the range of data transmission through air by monitoring the RSSI
372 and live data stream as the receiving antenna was deployed at a fixed site and Cryoegg hand-carried
373 over a distance of 1.6 km. A hand-held GPS receiver was used to record the position of Cryoegg as it
374 was carried, and the fixed position of the Cryoegg receiver.



376

377 Fig. 5 – topographic map of Switzerland showing location of the Rhône Glacier

378

379 The Rhône Glacier is located at N46°34.32' E8°22.58' in the Swiss Alps and is one of the most studied
380 glaciers, with records of front position dating back to the 17th Century (Church and others, 2019). The
381 16 km² glacier is at the pressure melting point throughout and there is an active subglacial drainage
382 network. The glacier is the focus of an intensive subglacial monitoring project, with artificial moulins
383 drilled via hot water in 2018. The moulins remained active in August 2019, when we deployed Cryoegg
384 on the end of a rope tether.

385 Salt dilution gauging (Moore, 2005) was used to estimate moulin discharge. A known quantity of
386 tracer, sodium chloride (NaCl, “table salt”) was added to the supraglacial stream approximately 25 m
387 upstream of the moulin. The discharge can then be calculated from EC readings and the concentration
388 of NaCl added. EC was measured in the supraglacial stream by a Keller DCX-22-CTD 15 m upstream of
389 the moulin and also recorded and transmitted once per second by a Cryoegg lowered into water at
390 the bottom of the moulin.

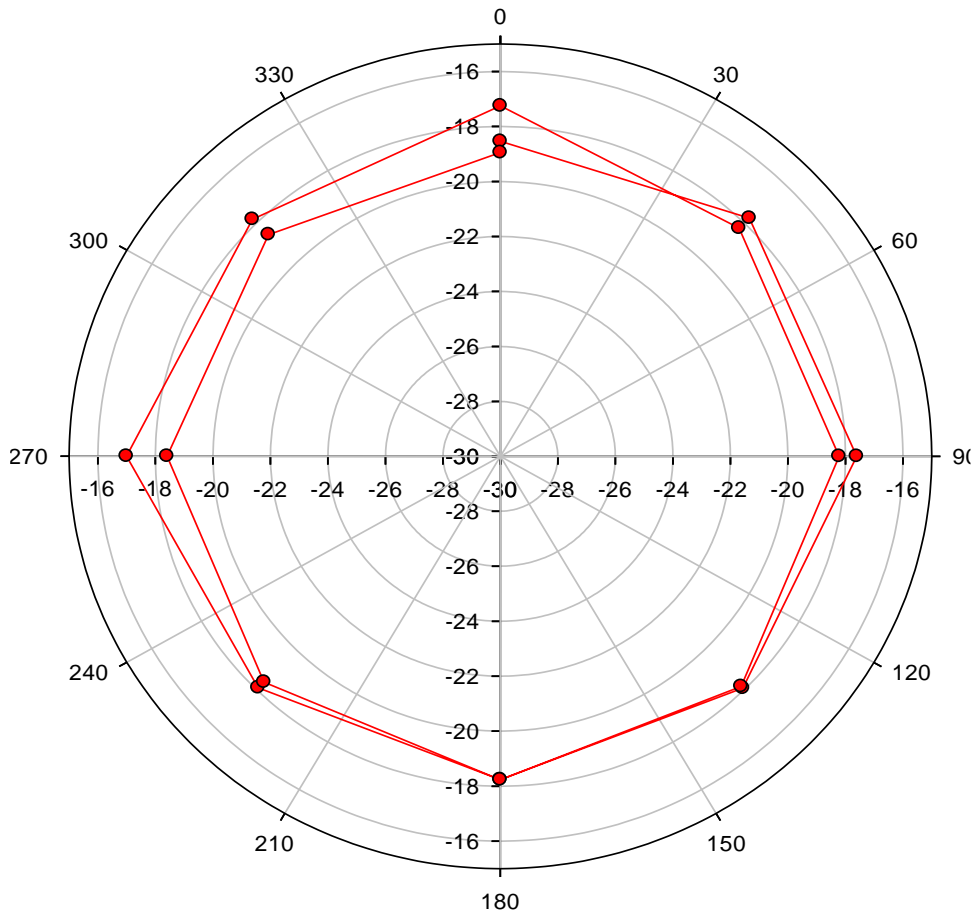
391

392 **RESULTS**

393 **Laboratory RF tests**

394

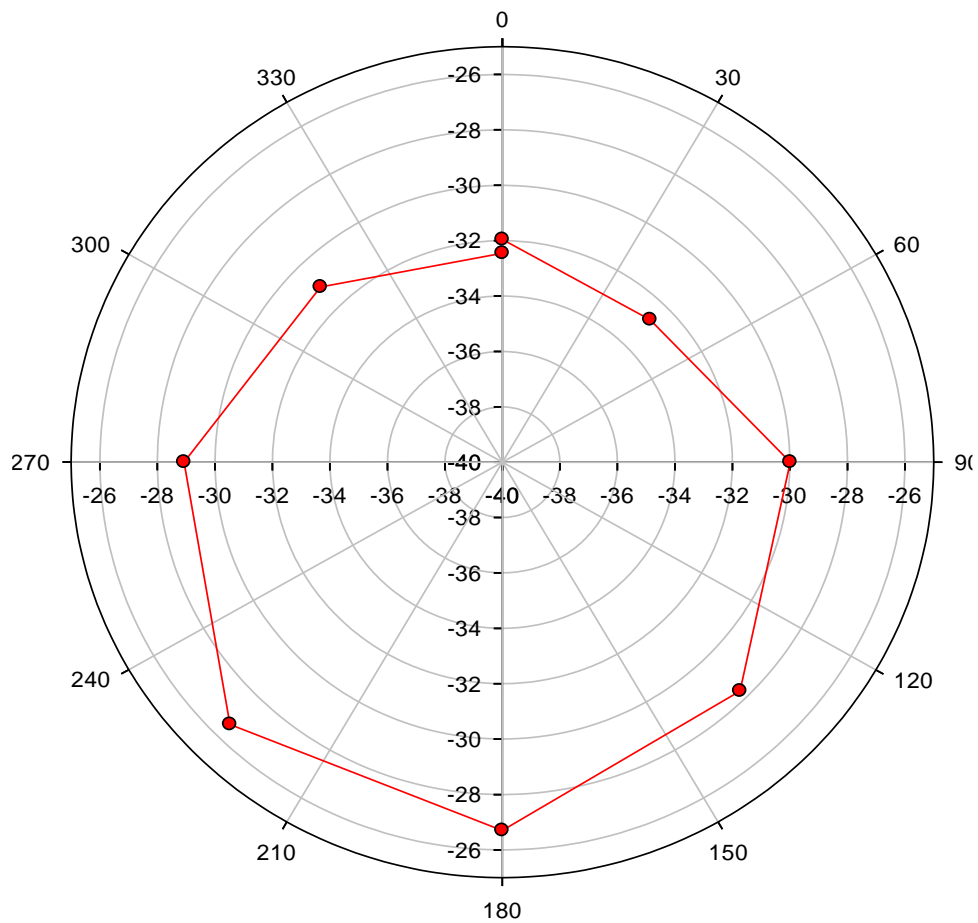
395 RF power meter assessments confirmed the assumption (Table 3) that the transmitter put out the full
396 +27 dBm (0.5 W) during each transmission.



397

398 Fig. 6 – Horizontal radiation pattern of Cryoegg measured in the RF test chamber

399 The horizontal radiation pattern was measured at eight points around the circumference and is shown
400 in Fig. 6. For this measurement the receiving antenna (a log-periodic) was vertically polarised (a brief
401 check showed that this gave a larger signal than when horizontally polarised) and Cryoegg was
402 orientated with its case split line horizontal. Two complete revolutions were measured to check
403 consistency. The pattern is largely omnidirectional, with <2 dB of variation between all the
404 measurements.



405

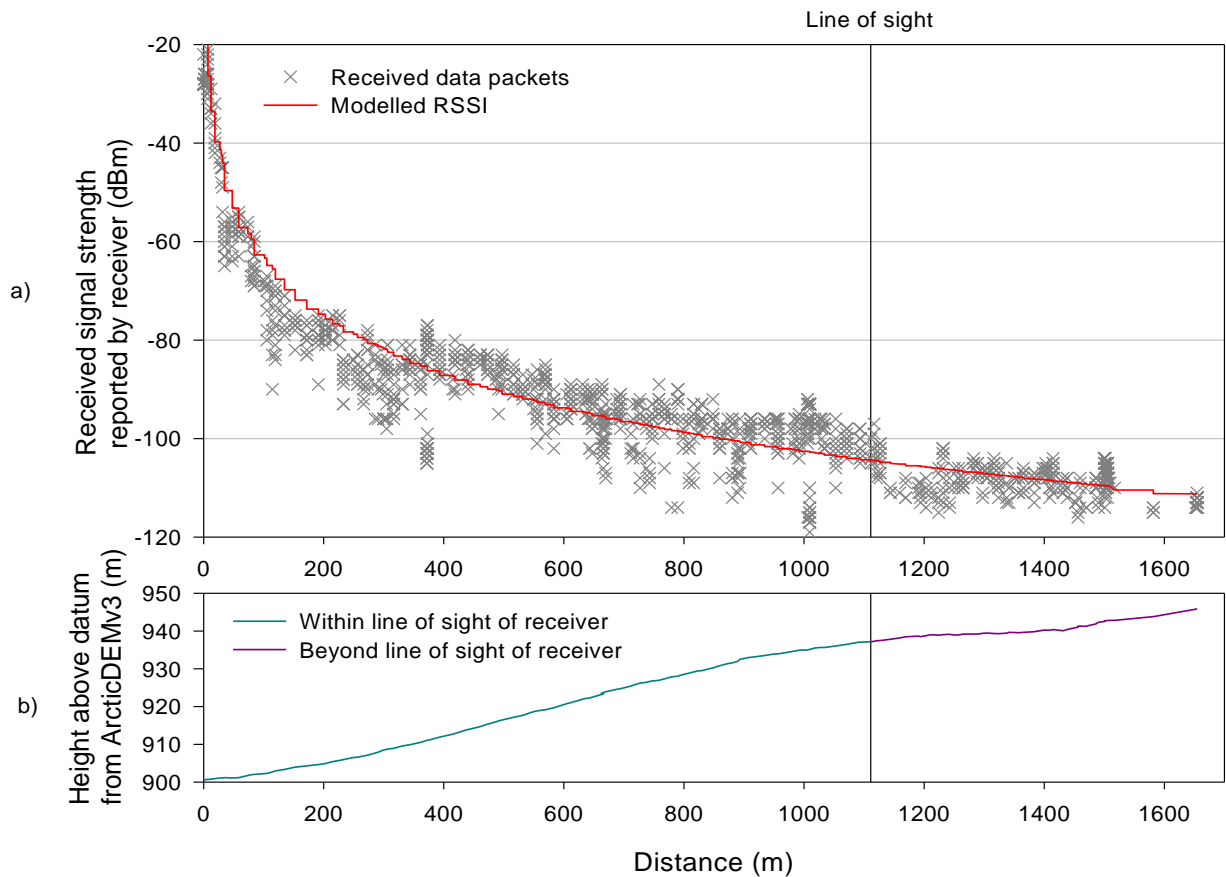
406 Fig. 7 – Vertical radiation pattern of Cryoegg measured in the RF test chamber

407 To simulate the RF performance in the borehole, we re-oriented the Cryoegg to have the same
 408 orientation as it would have in the borehole, with the split line vertical and normal to the receiving
 409 antenna boresight – i.e. with the crown of the upper half pointing towards the receiving antenna, and
 410 the sensor ports pointing away. The receiving antenna was vertically polarised. The results in Fig. 7
 411 show that the signal level is significantly lower (10-12 dB) than in the horizontal plane, and that the
 412 pattern is not omnidirectional; there is a 6 dB variation as the unit is rotated.

413

414

415 Surface propagation at Sermeq Kujalleq (Store Glacier)



416

417 Fig. 8 – a) RSSI recorded by receiver during surface range test at Sermeq Kujalleq (Store Glacier) and
 418 modelled received signal strength.). b) shows the ground elevation (height above the WGS84 ellipsoid)
 419 along the route taken. The black vertical line in both plots shows the point where the transmitter went
 420 beyond the line of sight to the receiver due to the ice sheet's surface topography.

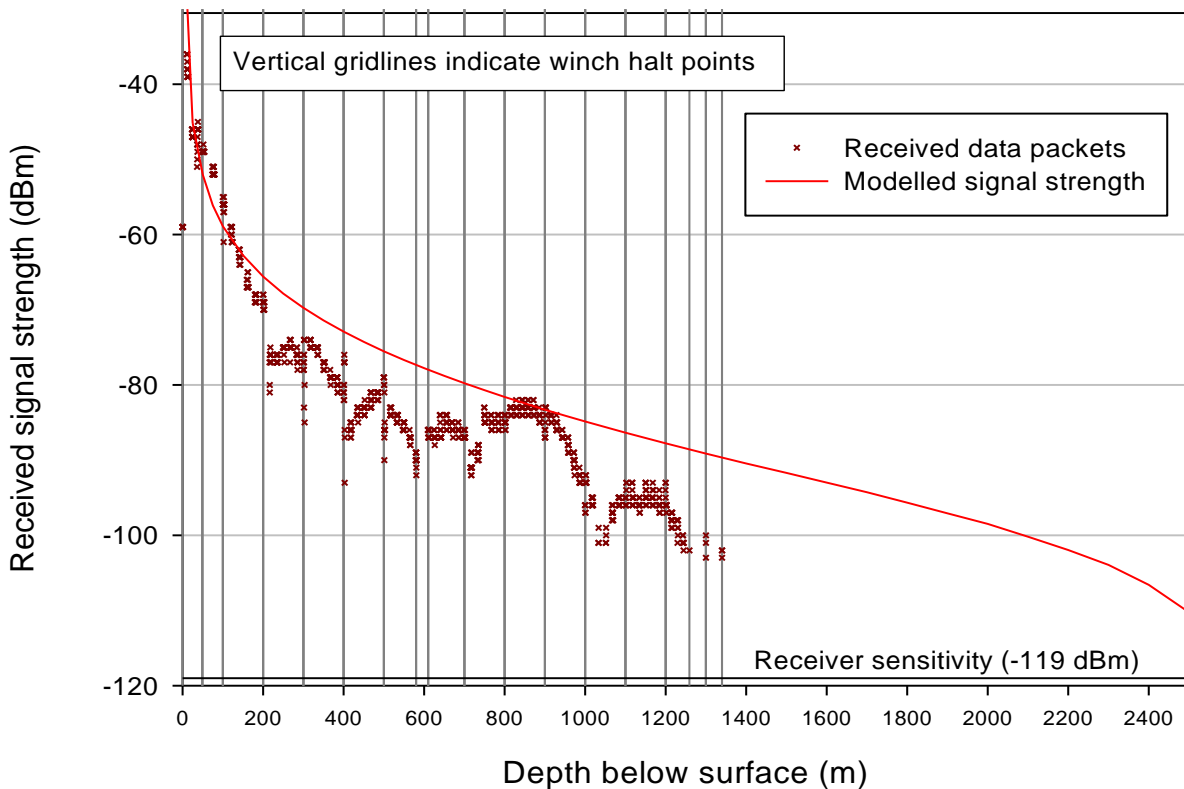
421 Fig. 8a shows recorded signal strength for successfully received data packets against range from the
 422 receiver. The terrain profile in Fig. 8b was produced from ArcticDEM v3
 423 (<https://doi.org/10.7910/DVN/OHHUKH>) 2 m mosaic values extracted to match the GPS positions
 424 recorded in the field. A line-of-sight binary was calculated using the QGIS visibility analysis plugin with
 425 the receiver height set at 1.5 m and the transmitter height at 1 m.

426 **Deployment at Sermeq Kujalleq (Store Glacier)**

427 Cryoegg was lowered into a hot water drilled borehole and a moulin. One deployment attempt was
 428 made in the hot water drilled borehole, but the borehole proved too narrow for Cryoegg to pass
 429 through. One data point was obtained with Cryoegg in the borehole about 400 m below the surface,
 430 but it was impossible to proceed further because of borehole refreezing. Moulin deployment was
 431 attempted in a very large moulin (measured at $4.3 \text{ m}^3\text{s}^{-1}$ discharge at the time of deployment) adjacent
 432 to the drill site. Cryoegg was caught in a series of plunge pools and eventually the force of the water
 433 caused it to break free from its tether and it was rapidly swept away out of range. We only obtained
 434 a few data points before losing the signal.

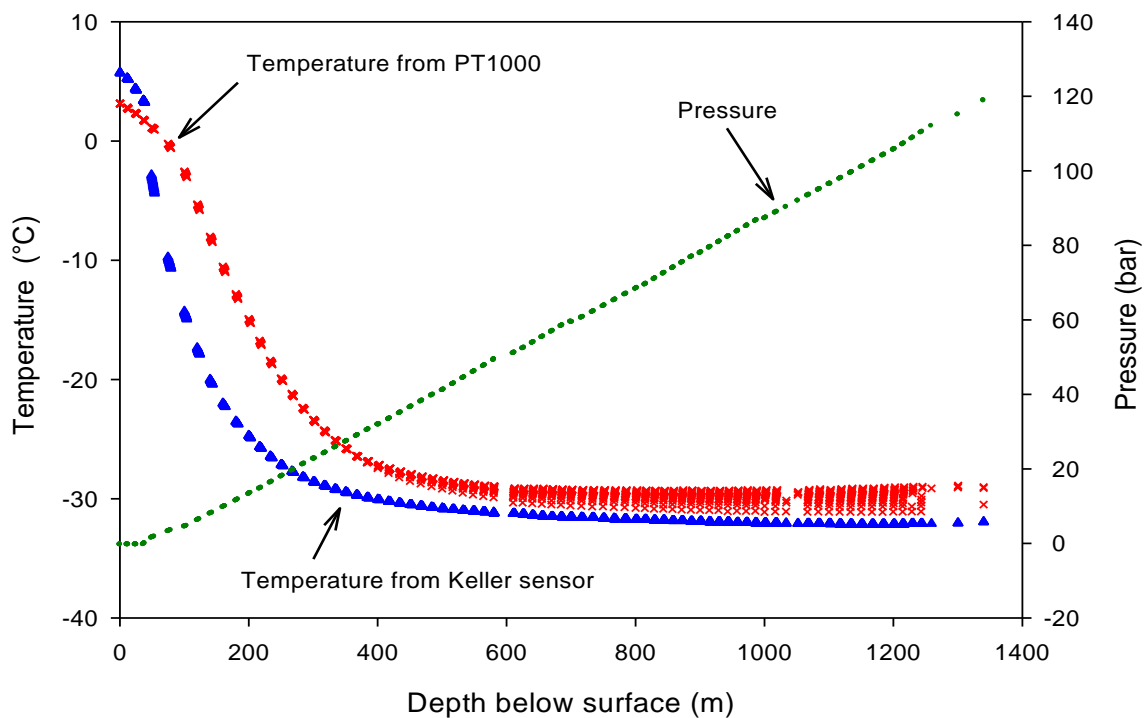
435 Downhole propagation at EastGRIP

436 At EastGRIP, the borehole is filled with ESTISOL 240 drill fluid rather than water (Sheldon and others,
437 2014). Previous tests at the site (Bagshaw and others, 2018) demonstrated that the fluid had minimal
438 impact on signal propagation. Fig. 9 shows the RSSI plotted against depth. Depth is linearly
439 interpolated between depth-measured winch halt points (shown as vertical gridlines on Fig. 9), which
440 is a fair assumption because the winch motor speed was constant between these halts. The firmware
441 was configured to produce a burst of 16 packets, one per second, and then wait for 60 seconds before
442 the next burst. This accounts for the clustered data points on Fig. 9, as all the successfully received
443 packets are plotted. There are large variations (>10 dB) in signal level at 300, 400 and 500 m, coinciding
444 with the point where the winch was halted, and even retrograde paths, for example between 400 and
445 500 m; 700-850 m; 1000-1100 m. The deepest point at which packets were successfully received was
446 1340m below the surface. No packets were received as Cryoegg was pulled back up to the surface.
447 When Cryoegg was retrieved, it was found to be full of drill fluid, indicating that it had leaked under
448 pressure.



449

450 Fig. 9 – Received signal strength of successfully-received data packets during a test in the EastGRIP
451 borehole, together with modelled signal strength (explained in “radioglaciological implications”
452 section)



453

454

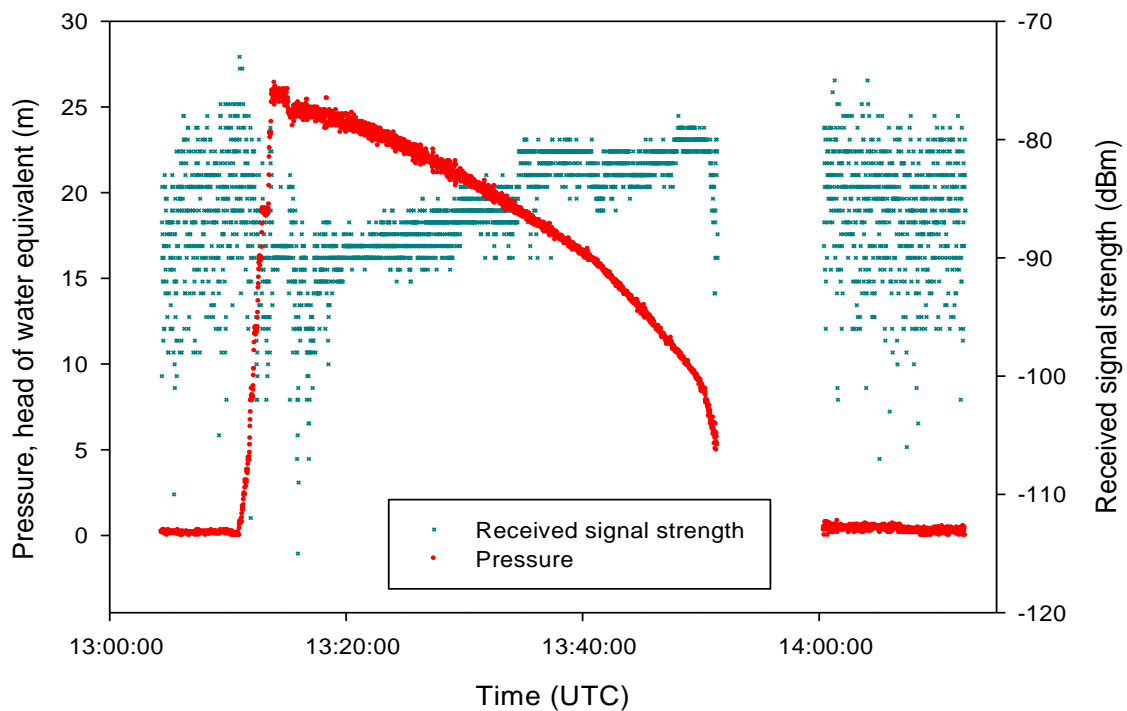
455 Fig. 10 – Cryoegg sensor data received at the surface during deployment into the EastGRIP borehole.

456 The hydrostatic pressure increased with depth (Fig. 10) – the small offset is because the drill fluid is
 457 around 50 m below the surface level. Data was obtained down to 1340 m, although significant packet
 458 loss occurred beyond 1250 m. The two temperature plots represent data from the two different
 459 temperature sensors. The Pt1000 sensor is inside the case, hence it records a higher temperature for
 460 a given depth when compared with the Keller, which has direct contact with the drill fluid. The
 461 conversion equation from the Pt1000 reported value (which is in arbitrary units) to temperature is
 462 based on theory and has not been confirmed by calibration. Since the primary test objective was to
 463 test the radio link, we did not prioritise calibrating the temperature sensors prior to the field
 464 deployment. The high degree of clustering of the data points from the Keller sensor suggests that it
 465 contains some internal averaging, although this may be caused by the significant mass of the sensor
 466 body itself. Cryoegg was at ambient ice surface temperature before entering the borehole, so the
 467 majority of the temperature data recorded here is simply the instrument cooling down to the ambient
 468 englacial temperature. The spread in Pt1000 temperature results beyond 400m depth is caused by
 469 self-heating of the sensor due to repeated measurements in quick succession, which becomes
 470 apparent once Cryoegg has cooled to the ambient englacial temperature.

471

472 **Moulin drainage at Rhône Glacier**

473 Cryoegg did not reach the bed of the Rhône Glacier, 200m below the surface, via the moulin and
474 instead appeared to be in a deep plunge pool 150m below the surface. Pressure readings received
475 from Cryoegg in real time confirmed that it was in up to 25m deep water. Fig. 11 shows the pressure
476 recorded whilst Cryoegg was in the plunge pool, and the corresponding received signal strength. There
477 was a sharp rise in pressure as Cryoegg was lowered into the water at 13:12:00 UTC and then a gradual
478 decline over the next 40 minutes. The gap in the data centred on 13:55 was an interruption in the data
479 logging. After the logging resumed, the water pressure had fallen to atmospheric pressure. The
480 reduction in water pressure coincided with a 10dB increase in received signal strength over the same
481 period.



482

483 Fig. 11 – Pressure and received signal strength from Cryoegg in a moulin on Rhône Glacier, 15th
484 August 2019

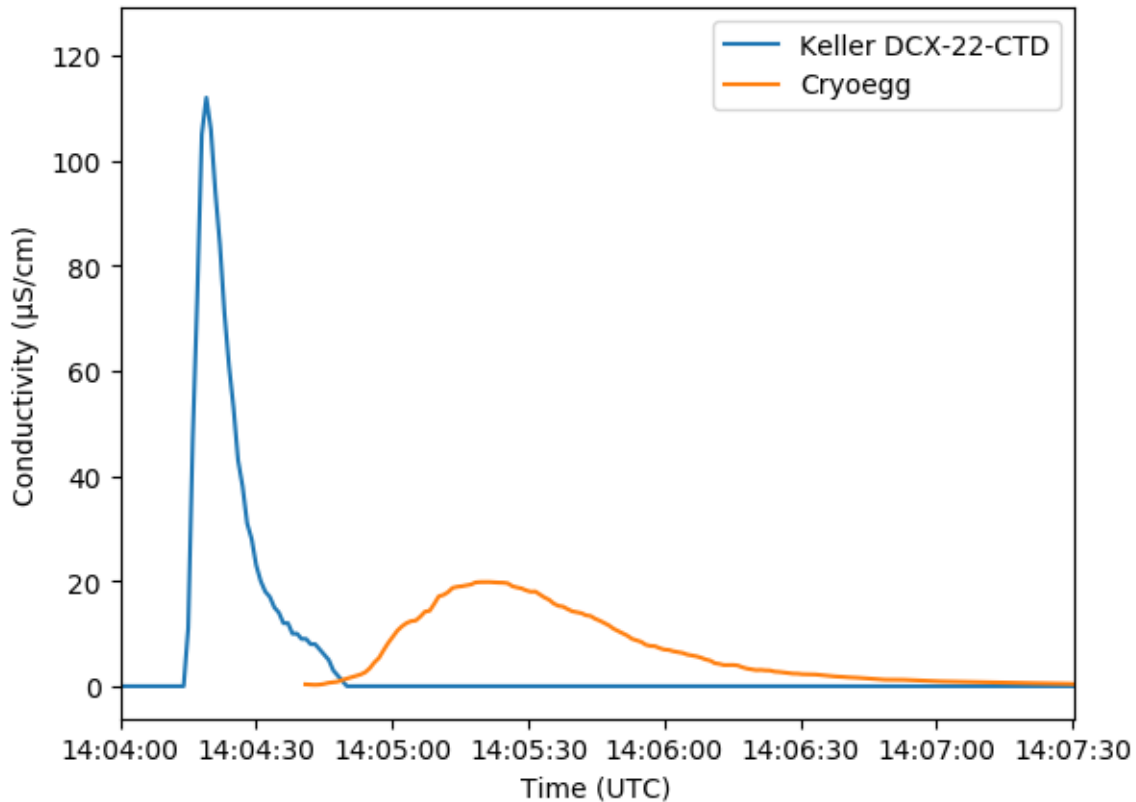
485

486

487 Salt discharge gauging at Rhône Glacier

488 The salt discharge gauging experiment at Rhône Glacier consisted of injecting a 100 g l⁻¹ NaCl salt
489 solution into a supraglacial stream, 25m upstream from a moulin. A Keller DCX-22-CTD in the
490 supraglacial stream, 10m downstream from the injection point, measured the EC in the stream.
491 Simultaneously, a Cryoegg in the moulin plunge pool (150m below the ice surface) measured the EC
492 and transmitted the measurements to the surface in real time.

493 Fig. 12 shows the results from the Keller logger in the stream alongside the results from Cryoegg in
494 the moulin.



495

496 Fig. 12 – comparison of salt wave passing Keller logger in the supraglacial stream with Cryoegg
497 within the moulin. 15th August 2019.

498 The discharge of the supraglacial stream was calculated by the salt dilution as 104 litres s⁻¹ (Moore,
499 2005), and the discharge within the moulin was slightly higher at 113 litres s⁻¹. The time between the
500 two peaks was 60 seconds. The velocity of the water between the two instruments was 2.75 m s⁻¹
501 based on the transit time and the distance between them (15 m in the stream + 150 m down the
502 moulin = 165 m).

503

504 DISCUSSION

505 Radioglaciological implications

506 *Surface range test*

507 The main objective of field testing was to verify the performance of Cryoegg in a real glacial
508 environment. The surface range test at Sermeq Kujalleq/Store Glacier (Fig. 8) confirmed that the
509 radiated output of Cryoegg matched our design calculations. We modelled the expected RSSI using
510 the conventional two-ray ground-reflection model (Bullington, 1947) used for VHF propagation. The
511 transmitter and receiver heights required were modelled using the DEM profile shown in Fig. 8b. The
512 transmitter and receiver parameters in the model were those from the link budget in Table 3. The
513 model produces a good fit to the real data, confirming that the parameters were indeed realistic
514 estimates. The variations in the signal strength data are because the DEM profile is derived from data
515 with a 2m resolution of the glacier surface terrain - but the glacier surface had undulations of around
516 0.5-1m in height. This caused variations in antenna height during the test that are not reflected in the
517 DEM profile. The later part of the test was beyond the line of sight to the receiver (as shown by the
518 elevation profile in Fig. 8b), which accounts for the step reduction in signal strength beyond 1100 m.

519 *EastGRIP borehole test*

520 The test in the EastGRIP borehole was intended to verify both the mechanical and electrical
521 performance of Cryoegg in a simulated deployment, and demonstrate the radio link through deep
522 glacial ice. No data was received beyond 1340 m depth and on return to the surface Cryoegg was
523 found to have failed and stopped transmitting. This appears to have been a mechanical failure. Drill
524 fluid was found in the Cryoegg housing after the tests. The fluid is non-conductive and so should not
525 have caused any electrical damage, but the hydrostatic pressure is likely to have affected some
526 components. The most likely failure points are the battery (which being a soft "pouch cell" type has
527 no protection from pressure) and its connectors, which may be forced apart by non-conductive fluid
528 under high pressure, breaking the circuit.

529 An important question remains: if the leak had not occurred and Cryoegg had continued operating
530 down to the bottom of the borehole (2000 m down), would we have received data at that depth? To
531 determine this, we estimate the RF performance based on the recorded data.

532 The receiver sensitivity (the minimum decodable signal strength) is -119 dBm (1.25 fW), and in other
533 range tests (Fig. 8) we succeeded in decoding signals down to this level (RC1701xx-MBUS Datasheet,
534 2018). However, the RSSI data for the EastGRIP borehole (Fig. 9) show that the weakest signals
535 received were at -103 dBm, 16 dB above the minimum receivable level. This suggests the system would
536 have continued working beyond 1340 metres depth without the mechanical failure. To forecast signal
537 levels at greater depth, we modelled the expected RSSI in the borehole. The model is based on the
538 same method as for the link budget in Table 3, but with ice attenuation calculated based on the
539 glacier's internal temperature at each depth rather than assuming a constant value at all depths.

540 The temperature profile of the EastGRIP borehole was measured in July 2019 using the University of
541 Copenhagen's automated logger (Gundrestup and others, 1994). We applied the temperature
542 measurements to an attenuation model (MacGregor and others, 2007, 2015) to give an estimate for
543 the ice-related attenuation down to 2100m below the surface (Fig. 9). To continue the temperature
544 profile to the glacier bed depth (2500m) we conjectured that the temperature would rise rapidly to
545 reach 0 °C at the bed, by analogy with the temperature profile at NorthGRIP (Dahl-Jensen and others,
546 2003). This represents a worst-case since the model produces very high attenuation (69 dB km⁻¹) at

547 0 °C. This produces a profile with relatively low attenuation ($\sim 7\text{dB km}^{-1}$) in the coldest part of the
548 glacier, increasing rapidly at the surface and bed where the ice is warmer.

549 When we initially developed the model, we found that using the value of -15dBi for the transmit
550 antenna gain (which produced a good fit to the surface range test data) overestimated the RSSI in the
551 borehole, even at points very close to the surface. This suggests that the radiated signal from Cryoegg
552 was much lower in the borehole when compared to the surface range test. It is likely that the antenna
553 performance was affected by the substantial metal apparatus on the winch cable just above where
554 Cryoegg was attached. The dielectric constant of the drill fluid is not the same as in air and this may
555 also have affected the antenna matching. Consequently, we reduced the transmit antenna gain by
556 20dB (to -35dBi) in the model to produce a result that more closely fits the observed data. The final
557 model output with the reduced transmit gain is plotted in Fig. 9.

558 The modelled signal strength is higher than the real data at most depths (Fig. 9), although it matches
559 the peak between 800 and 900 m, and there are two further effects that help explain why.

560 Firstly, the large ($>10\text{ dB}$) variation in signal strength observed at several winch halt points is most
561 likely caused by Cryoegg rotating on the vertical axis as the wire rope twists. Cryoegg was oriented
562 with its split line horizontal during these tests, meaning that the transmitting antenna is oriented in
563 an end-fire mode towards the receiver. The deceleration of the winch will result in some of the
564 momentum of Cryoegg and the cable being converted into torsional forces on the winch cable, with
565 Cryoegg twisting back and forth on the end of the cable. This will affect the radiation from the antenna
566 because the radiation pattern seen by the receiving antenna is not uniform (Fig. 7). It is plausible that
567 the retrograde slope of the signal strength between 400 and 500m is caused by Cryoegg slowly
568 rotating on the winch cable, given the signal variation is comparable to that seen during the 400m and
569 500m winch halts.

570 Secondly, birefringence likely impacted the signal. Birefringence is a phenomenon exhibited by many
571 crystalline materials, where the refractive index varies depending on the polarisation and direction of
572 propagation of electromagnetic waves. Glacier ice affects the polarisation of VHF radio waves through
573 birefringence, and radar studies use this effect to infer details about the crystal fabric of the glacier
574 ice (Hargreaves, 1978; Li and others, 2018). Birefringence splits the wave from Cryoegg into two
575 elliptically-polarised waves of opposing chirality with differing phase velocities. The relative phase
576 delay between the two waves appears at the receiver as an apparent change in polarisation, and
577 therefore it is possible that the wave could arrive at the receiving antenna on the opposite polarisation
578 to the antenna, resulting in a “null” – a significant reduction in received signal strength. Since this
579 phase delay relates to distance travelled through the medium, this effect would produce nulls at
580 specific depths corresponding to relative phase delays of 180 degrees. The signal strength plot (Fig. 9)
581 appears to show a number of nulls– notably at around 600 m and 1040 m, which are most likely caused
582 by birefringence. Multipath reflection effects, such as when the signal reflected off a surface interferes
583 destructively with the direct signal at the receiver (Griffiths, 1987, 102–104), are the other possible
584 explanation, but these can be discounted because there is no obvious candidate for the reflecting
585 surface. The geometry required to produce widely-spaced large nulls rules out horizontal reflectors
586 like the glacier bed or internal layers, and the shear margin is too far away (5 km) to produce this type
587 of null.

588 The axial rotation of Cryoegg and the birefringent effects may also act in concert, which would explain
589 why the signal variations are so large at some of the winch halt points ($>10\text{ dB}$ at most locations).
590 These two effects explain why the signal level drops below the modelled values: the model assumes
591 constant antenna gain and matched polarisation, whereas in the real data the orientation varies

592 (altering the transmit antenna gain) and the birefringence means that a proportion of the signal power
593 is transferred to the opposite polarisation and is lost to the receiver.

594 The birefringent effect could be mitigated against in future development by feeding the output of
595 each of the two crossed receiving antennas into a two-channel diversity receiver, which would then
596 be able to decode the signal regardless of its polarisation. This polarisation diversity technique has
597 previously been demonstrated mitigating polarisation nulls in HF ionospheric radio links (Stott, 2005)
598 where magnetoionic effects produce polarisation changes which are analogous to those produced by
599 birefringence (Davies, 1990).

600 *Rhône glacier moulin test*

601 The performance of the radio link in the Rhône glacier moulin (Fig. 11) was satisfactory. We anticipated
602 that the temperate ice and presence of flowing water would increase the overall attenuation. Fig. 11
603 shows that the signal propagating through 25 m of meltwater and a further 125 m of temperate ice to
604 the glacier surface was attenuated to -90 dBm. This compares with the EastGRIP borehole (Fig. 9)
605 where this signal strength was reached after more than 500 m. The reduction in observed moulin
606 water pressure, indicative of 25m head of water draining out of the moulin, produced an increase in
607 RSSI by around 10 dB. This confirms that the presence of liquid water increases the signal attenuation.

608 The variation in signal is much greater when Cryoegg is in the “atmospheric pressure” region of the
609 moulin rather than when it is in >1 m of water (Fig. 11). When Cryoegg is reporting pressure close to
610 atmospheric pressure, it is being splashed by the water, or water is flowing smoothly past it. In this
611 scenario the water flow will spin and agitate Cryoegg on the end of the rope, creating variation in
612 signal level because of the antenna pattern. The turbulent flow of the water will also create ever-
613 changing levels of attenuation. However, once Cryoegg is below the water surface, the viscosity of the
614 water will reduce its spinning and agitation, and the attenuation due to the water will be constant.

615

616 **Glaciohydrological implications**

617 The water pressure recorded by Cryoegg in the moulin steadily decreased during the 40 minutes that
618 it remained in the plunge pool (Fig. 11). Eventually, the water level dropped below the Cryoegg and it
619 returned to atmospheric pressure with the characteristic fluctuations in RSSI caused by splashing
620 water. We interpret this as dynamic drainage of the plunge pool over the afternoon, as water backed
621 up in the drainage system forces its way to the glacier bed. Similar pressure variations have been
622 previously observed in moulins (Iken, 1972; Röthlisberger, 1980; Holmlund and Hooke, 1983) and
623 demonstrate that the subglacial drainage system is not in equilibrium but constantly fluctuating
624 (Röthlisberger and Lang, 1987). The characteristic step-pool system develops if the moulin persists for
625 more than one season (Gulley, 2009); the artificial moulin was drilled directly to the end in 2018, but
626 by 2019 was 'kinked' and a plunge pool formed approximately 50 m above the bed.

627 Simultaneous salt tracing in a supraglacial stream feeding the moulin and within the moulin itself
628 shows (Fig. 12) that the moulin discharge was slightly higher than the stream discharge – unsurprising,
629 as the stream that we measured was not the sole supply of water feeding the moulin. This experiment
630 demonstrates Cryoegg's potential for measuring hydrological parameters in locations that are difficult
631 to access. Previously, moulin discharge has been estimated at the surface (either by field
632 measurements or remote sensing), which masks the effect of water being stored within the vertical
633 column of the moulin itself (Werder and others, 2010). We show that it is possible to monitor
634 supraglacial discharge, the height of the stored water column within the moulin, and the moulin
635 discharge simultaneously and in real time, providing a valuable new approach for future studies of
636 glacier hydrology.

637 **Comparison with other wireless subglacial probes**

638 The most successful wireless subglacial probe for deep ice has been the WiSe system (Smeets and
639 others, 2012). This was demonstrated returning a signal through 2500 m of ice in Greenland. This
640 system operated at 30 MHz in order to benefit from lower free-space path loss, but at the expense of
641 making the antennas very large. The WiSe system suffered from some skywave interference affecting
642 signal reception, which is a particular issue at 30 MHz and below, and required use of a large (5 m
643 long) HB9CV type antenna to mitigate against it. WiSe required a 1 W (+30 dBm) transmitter to
644 communicate at depths of more than 2000 m, but it is not clear how much of this power was actually
645 radiated – the ferrite-loaded antenna used was likely to be very lossy.

646 The GlacsWeb system originally operated at 433 MHz (Martinez and others, 2004) but later (Martinez
647 and others, 2013) used 151 MHz, giving a maximum reported range in ice of 70 m (Hart and others,
648 2019). Cryoegg is specifically designed for deep ice, and hence its radio performance greatly exceeds
649 that of GlacsWeb, enabling its use in at least 1000 m of ice. Our probe and receiving antenna are both
650 more compact than the WiSe system and we use commercially-available radio modules that adhere
651 to an international open standard, which means that the key components are likely to be readily
652 available well into the future.

653 **CONCLUSION AND OUTLOOK**

654 We have undertaken a full re-design of the wireless subglacial sensor platform Cryoegg, using a new
655 radio link technology and improved link budget design, and demonstrate that it can transmit sensor
656 data in real time through more than 1.3 km of cold ice. Deployments in moulins in temperate ice show
657 that Cryoegg is a valuable tool for recording englacial and subglacial hydrological properties in situ,
658 and hence giving further insight into processes in these environments. The EC sensor, originally
659 intended as a proxy for total dissolved solids in subglacial water, can facilitate salt dilution gauging for

660 real-time estimates of discharge. All sensors operated well, revealing englacial conditions and
661 demonstrating their applicability for future subglacial deployments. The sensors fitted to the existing
662 design were chosen because of their ease of implementation and their applicability to studies of
663 subglacial hydrology, but Cryoegg can be adapted to support other sensors.

664 Future developments will refine and enhance the design, particularly with respect to the antenna
665 performance and mechanical design, so that we have a robust instrument capable of returning data
666 for months or years through 2.5 km of ice. This would enable us to match the performance of the WiSe
667 system (Smeets and others, 2012) but with more compact antennas, enabling the Cryoegg to ‘roam’
668 through englacial and subglacial hydrological systems to collect spatially and temporally distributed
669 measurements, reported in real time. Cryoegg technology will also be adapted for englacial studies in
670 irregular and refreezing hot-water-drilled boreholes, by creating a cylindrical form factor with a much
671 smaller diameter than Cryoegg, allowing deployment in a smaller borehole.

672 **ACKNOWLEDGEMENTS**

673 This work was funded by UK Engineering and Physical Sciences Research Council (EPSRC) New
674 Investigator Award EP/R03530X/1, awarded to Liz Bagshaw.

675 Thanks to all who assisted us in the field, in particular: Trevor Popp, Romain Duphil and the EastGRIP
676 drill team; “Mickey” MacKay, Eliza Dawson and Rob Law at the RESPONDER site; Lai Bun Lok, Jonathan
677 Hawkins, the ETH Zürich VAW Glaciology team and the Swiss Air Force at the Rhône Glacier site. Phil
678 Anderson gave us use of the RF test chamber. We are grateful for in-kind contributions of equipment
679 from Quadro and Radiocrafts. Particular thanks to the team at DGF Engineering for the machining of
680 the caseworks, to Protronix EMS Ltd for the rapid production of the electronics, and to Justin Johnson
681 of InnovAntennas for the custom design of the receiving antenna. Miles Gould provided assistance
682 with the algebra for Equation 3. We would particularly like to thank our anonymous reviewers for their
683 helpful contributions and suggestions.

684 EastGRIP is directed and organized by the Center of Ice and Climate at the Niels Bohr Institute. It is
685 supported by funding agencies and institutions in Denmark (A. P. Møller Foundation, University of
686 Copenhagen), USA (US National Science Foundation, Office of Polar Programs), Germany (Alfred
687 Wegener Institute, Helmholtz Centre for Polar and Marine Research), Japan (National Institute of Polar
688 Research and Arctic Challenge for Sustainability), Norway (University of Bergen and Bergen Research
689 Foundation), Switzerland (Swiss National Science Foundation), France (French Polar Institute Paul-
690 Emile Victor, Institute for Geosciences and Environmental research) and China (Chinese Academy of
691 Sciences and Beijing Normal University)

692 Bryn Hubbard acknowledges support for hot-water borehole drilling from HEFCW through a Capital
693 Equipment Grant awarded to Aberystwyth University, and from the NERC through grant NE/K006126.

694 The RESPONDER project is funded by a Consolidator Grant to Poul Christoffersen from the European
695 Research Council, under the European Union’s Horizon 2020 research and innovation programme
696 (Grant 683043).

697 Tom Chudley was supported by a Natural Environment Research Council Doctoral Training Partnership
698 Studentship (Grant NE/L002507/1).

699 ArcticDEM was created from DigitalGlobe, Inc., imagery and funded under National Science
700 Foundation awards 1043681, 1559691, and 1542736

701

702 REFERENCES

703

- 704 Bagshaw E and 10 others (2018) Utilising Wireless Sensor Technologies in Glaciology. *Paper*
705 *presented at AGU Fall Meeting 2018*. Washington, DC
706 <http://adsabs.harvard.edu/abs/2018AGUFM.C43D1823B>
- 707 Bagshaw EA and 6 others (2014) Novel wireless sensors for in situ measurement of sub-ice
708 hydrologic systems. *Annals of Glaciology* **55**(65), 41–50 (doi:10.3189/2014AoG65A007)
- 709 Bagshaw EA and 7 others (2012) E-tracers: Development of a low cost wireless technique for
710 exploring sub-surface hydrological systems. *Hydrological Processes* **26**(20), 3157–3160
711 (doi:10.1002/hyp.9451)
- 712 Barrella T, Barwick S and Saltzberg D (2011) Ross Ice Shelf in situ radio-frequency ice attenuation.
713 *Journal of Glaciology* **57**(201), 61–66 (doi:10.3189/002214311795306691)
- 714 Barwick S, Besson D, Gorham P and Saltzberg D (2005) South Polar in situ radio-frequency ice
715 attenuation. *Journal of Glaciology* **51**(173), 231–238 (doi:10.3189/172756505781829467)
- 716 van den Broeke MR and 7 others (2016) On the recent contribution of the Greenland ice sheet to sea
717 level change. *The Cryosphere* **10**(5), 1933–1946 (doi:10.5194/tc-10-1933-2016)
- 718 Bullington K (1947) Radio Propagation at Frequencies above 30 Megacycles. *Proceedings of the*
719 *Institute of Radio Engineers* **35**(10), 1122–1136 (doi:10.1109/JRPROC.1947.232600)
- 720 Chandler DM and 11 others (2013) Evolution of the subglacial drainage system beneath the
721 Greenland Ice Sheet revealed by tracers. *Nature Geoscience* **6**(3), 195–198
722 (doi:10.1038/ngeo1737)
- 723 Chu VW (2014) Greenland ice sheet hydrology: A review. *Progress in Physical Geography: Earth and*
724 *Environment* **38**(1), 19–54 (doi:10.1177/0309133313507075)
- 725 Chudley TR and 6 others (2019) Supraglacial lake drainage at a fast-flowing Greenlandic outlet
726 glacier. *Proceedings of the National Academy of Sciences* **116**(51), 25468–25477
727 (doi:10.1073/pnas.1913685116)
- 728 Church G, Bauder A, Grab M, Rabenstein L, Singh S and Maurer H (2019) Detecting and
729 characterising an englacial conduit network within a temperate Swiss glacier using active
730 seismic, ground penetrating radar and borehole analysis. *Annals of Glaciology* **60**(79), 193–
731 205 (doi:10.1017/aog.2019.19)
- 732 Clarke GKC (1987) Subglacial till: A physical framework for its properties and processes. *Journal of*
733 *Geophysical Research: Solid Earth* **92**(B9), 9023–9036 (doi:10.1029/JB092iB09p09023)
- 734 Dahl-Jensen D, Gundestrup N, Gogineni SP and Miller H (2003) Basal melt at NorthGRIP modeled
735 from borehole, ice-core and radio-echo sounder observations. *Annals of Glaciology* **37**, 207–
736 212 (doi:10.3189/172756403781815492)
- 737 Davies K (1990) *Ionospheric Radio (IEE Electromagnetic Waves Series, Vol. 31)*. The Institution of
738 Engineering and Technology, London, UK

- 739 Doyle SH and 7 others (2018) Physical Conditions of Fast Glacier Flow: 1. Measurements From
740 Boreholes Drilled to the Bed of Store Glacier, West Greenland. *Journal of Geophysical*
741 *Research: Earth Surface* **123**(2), 324–348 (doi:10.1002/2017JF004529)
- 742 European Committee for Standardisation (2013) *EN 13757-4:2013 - Communication systems for*
743 *meters and remote reading of meters. Wireless meter readout (Radio meter reading for*
744 *operation in SRD bands)*. [https://bsol.bsigroup.com/en/Bsol-Item-Detail-](https://bsol.bsigroup.com/en/Bsol-Item-Detail-Page/?pid=000000000030249978)
745 [Page/?pid=000000000030249978](https://bsol.bsigroup.com/en/Bsol-Item-Detail-Page/?pid=000000000030249978)
- 746 Flowers GE (2018) Hydrology and the future of the Greenland Ice Sheet. *Nature Communications*
747 **9**(1), 2729 (doi:10.1038/s41467-018-05002-0)
- 748 Friis HT (1946) A Note on a Simple Transmission Formula. *Proceedings of the Institute of Radio*
749 *Engineers* **34**(5), 254–256 (doi:10.1109/JRPROC.1946.234568)
- 750 Griffiths J (1987) *Radio wave propagation and antennas*. Prentice-Hall, Hemel Hempstead, UK
- 751 Gulley J (2009) Structural control of englacial conduits in the temperate Matanuska Glacier, Alaska,
752 USA. *Journal of Glaciology* **55**(192), 681–690 (doi:10.3189/002214309789470860)
- 753 Gundrestrup NS, Clausen HB and Hansen BL (1994) The UCPH borehole logger. *Memoirs of National*
754 *Institute of Polar Research Special Issue* **49**, 224–233 [https://icedrill.org/library/ucph-](https://icedrill.org/library/ucph-borehole-logger)
755 [borehole-logger](https://icedrill.org/library/ucph-borehole-logger)
- 756 Hargreaves ND (1978) The Radio-Frequency Birefringence of Polar Ice. *Journal of Glaciology* **21**(85),
757 301–313 (doi:10.3189/S0022143000033499)
- 758 Hart JK, Martinez K, Basford PJ, Clayton AI, Robson BA and Young DS (2019) Surface melt driven
759 summer diurnal and winter multi-day stick-slip motion and till sedimentology. *Nature*
760 *Communications* **10**(1), 1–11 (doi:10.1038/s41467-019-09547-6)
- 761 Hoffman MJ and 9 others (2016) Greenland subglacial drainage evolution regulated by weakly
762 connected regions of the bed. *Nature Communications* **7**(1), 1–12
763 (doi:10.1038/ncomms13903)
- 764 Hofstede C and 7 others (2018) Physical Conditions of Fast Glacier Flow: 2. Variable Extent of
765 Anisotropic Ice and Soft Basal Sediment From Seismic Reflection Data Acquired on Store
766 Glacier, West Greenland. *Journal of Geophysical Research: Earth Surface* **123**(2), 349–362
767 (doi:10.1002/2017JF004297)
- 768 Holmlund P and Hooke RLeb (1983) High Water-Pressure Events in Moulins, Storglaciären, Sweden.
769 *Geografiska Annaler: Series A, Physical Geography* **65**(1–2), 19–25
770 (doi:10.1080/04353676.1983.11880070)
- 771 Hubbard BP, Sharp MJ, Willis IC, Nielsen MK and Smart CC (1995) Borehole water-level variations
772 and the structure of the subglacial hydrological system of Haut Glacier d’Arolla, Valais,
773 Switzerland. *Journal of Glaciology* **41**(139), 572–583 (doi:10.3189/S0022143000034894)
- 774 Iken A (1981) The Effect of the Subglacial Water Pressure on the Sliding Velocity of a Glacier in an
775 Idealized Numerical Model. *Journal of Glaciology* **27**(97), 407–421
776 (doi:10.3189/S0022143000011448)

- 777 Iken A (1972) Measurements of Water Pressure in Moulins as Part of a Movement Study of the
778 White Glacier, Axel Heiberg Island, Northwest Territories, Canada. *Journal of Glaciology*
779 **11**(61), 53–58 (doi:10.3189/S0022143000022486)
- 780 Iken A and Bindschadler RA (1986) Combined measurements of Subglacial Water Pressure and
781 Surface Velocity of Findelengletscher, Switzerland: Conclusions about Drainage System and
782 Sliding Mechanism. *Journal of Glaciology* **32**(110), 101–119
783 (doi:10.3189/S0022143000006936)
- 784 Iken A, Echelmeyer K, Harrison W and Funk M (1993) Mechanisms of fast flow in Jakobshavns Isbræ,
785 West Greenland: Part I. Measurements of temperature and water level in deep boreholes.
786 *Journal of Glaciology* **39**(131), 15–25 (doi:10.3189/S0022143000015689)
- 787 Joughin I (2017) MEaSURES Greenland Ice Velocity Annual Mosaics from SAR and Landsat, Version 1.
788 (doi:10.5067/OBXCG75U7540)
- 789 Joughin I, Smith BE, Howat IM, Scambos T and Moon T (2010) Greenland flow variability from ice-
790 sheet-wide velocity mapping. *Journal of Glaciology* **56**(197), 415–430
791 (doi:10.3189/002214310792447734)
- 792 Kamb B (1987) Glacier surge mechanism based on linked cavity configuration of the basal water
793 conduit system. *Journal of Geophysical Research: Solid Earth* **92**(B9), 9083–9100
794 (doi:10.1029/JB092iB09p09083)
- 795 Kamb B (1970) Sliding motion of glaciers: Theory and observation. *Reviews of Geophysics* **8**(4), 673–
796 728 (doi:10.1029/RG008i004p00673)
- 797 Karlsson NB and Dahl-Jensen D (2015) Response of the large-scale subglacial drainage system of
798 Northeast Greenland to surface elevation changes. *The Cryosphere* **9**(4), 1465–1479
799 (doi:10.5194/tc-9-1465-2015)
- 800 Lewis C and 6 others (2015) Airborne fine-resolution UHF radar: an approach to the study of
801 englacial reflections, firn compaction and ice attenuation rates. *Journal of Glaciology*
802 **61**(225), 89–100 (doi:10.3189/2015JoG14J089)
- 803 Li J and 8 others (2018) Multi-channel and multi-polarization radar measurements around the NEEM
804 site. *The Cryosphere* **12**(8), 2689–2705 (doi:10.5194/tc-12-2689-2018)
- 805 MacGregor JA and 11 others (2015) Radar attenuation and temperature within the Greenland Ice
806 Sheet. *Journal of Geophysical Research: Earth Surface* **120**(6), 983–1008
807 (doi:10.1002/2014JF003418)
- 808 MacGregor JA, Winebrenner DP, Conway H, Matsuoka K, Mayewski PA and Clow GD (2007)
809 Modeling englacial radar attenuation at Siple Dome, West Antarctica, using ice chemistry
810 and temperature data. *Journal of Geophysical Research: Earth Surface* **112**(F3)
811 (doi:10.1029/2006JF000717)
- 812 Martinez K, Basford PJ, Jager DD and Hart JK (2013) Using a heterogeneous sensor network to
813 monitor glacial movement. *Paper presented at 10th European Conference on Wireless Sensor*
814 *Networks*. <http://eprints.soton.ac.uk/348427/1/paper.pdf>

- 815 Martinez K, Ong R and Hart J (2004) Glacsweb: a sensor network for hostile environments. *2004 First*
816 *Annual IEEE Communications Society Conference on Sensor and Ad Hoc Communications and*
817 *Networks, 2004. IEEE SECON 2004.* 81–87 (doi:10.1109/SAHCN.2004.1381905)
- 818 Moore RD (2005) Introduction to salt dilution gauging for streamflow measurement Part 3: Slug
819 injection using salt in solution. *Streamline Watershed Management Bulletin* **8**(2), 1–6
- 820 Morlighem M and 31 others (2017) BedMachine v3: Complete Bed Topography and Ocean
821 Bathymetry Mapping of Greenland From Multibeam Echo Sounding Combined With Mass
822 Conservation. *Geophysical Research Letters* **44**(21), 11,051–11,061
823 (doi:10.1002/2017GL074954)
- 824 Ng FSL (2000) Canals under sediment-based ice sheets. *Annals of Glaciology* **30**, 146–152
825 (doi:10.3189/172756400781820633)
- 826 Nienow PW, Sole AJ, Slater DA and Cowton TR (2017) Recent Advances in Our Understanding of the
827 Role of Meltwater in the Greenland Ice Sheet System. *Current Climate Change Reports* **3**(4),
828 330–344 (doi:10.1007/s40641-017-0083-9)
- 829 Nienow PW and 6 others (2005) Hydrological controls on diurnal ice flow variability in valley glaciers.
830 *Journal of Geophysical Research: Earth Surface* **110**(F4) (doi:10.1029/2003JF000112)
- 831 Nye JF (1976) Water Flow in Glaciers: Jökulhlaups, Tunnels and Veins. *Journal of Glaciology* **17**(76),
832 181–207 (doi:10.3189/S002214300001354X)
- 833 Plewes LA and Hubbard B (2001) A review of the use of radio-echo sounding in glaciology: *Progress*
834 *in Physical Geography* (doi:10.1177/030913330102500203)
- 835 Pritchard HD, Arthern RJ, Vaughan DG and Edwards LA (2009) Extensive dynamic thinning on the
836 margins of the Greenland and Antarctic ice sheets. *Nature* **461**(7266), 971–975
837 (doi:10.1038/nature08471)
- 838 RC1701xx-MBUS Datasheet (2018) Radiocrafts AS, Oslo, Norway
839 https://radiocrafts.com/uploads/rc1701xx-mbus_datasheet.pdf
- 840 Röthlisberger H (1980) Gletscherbewegung und Wasserabfluss. *Wasser, Energie, Luft* **72**(9), 290–294
- 841 Röthlisberger H (1972) Water Pressure in Intra- and Subglacial Channels. *Journal of Glaciology*
842 **11**(62), 177–203 (doi:10.3189/S0022143000022188)
- 843 Röthlisberger H and Lang H (1987) Glacial Hydrology. *Glacio-Fluvial Sediment Transfer: An Alpine*
844 *Perspective*. Wiley, 207–84
- 845 Schoof C (2010) Ice-sheet acceleration driven by melt supply variability. *Nature* **468**(7325), 803–806
846 (doi:10.1038/nature09618)
- 847 Sheldon SG, Steffensen JP, Hansen SB, Popp TJ and Johnsen SJ (2014) The investigation and
848 experience of using ESTISOL™ 240 and COASOL™ for ice-core drilling. *Annals of Glaciology*
849 **55**(68), 219–232 (doi:10.3189/2014AoG68A036)
- 850 Smeets CJPP and 6 others (2012) A wireless subglacial probe for deep ice applications. *Journal of*
851 *Glaciology* **58**(211), 841–848 (doi:10.3189/2012JoG11J130)

- 852 Sole AJ and 6 others (2011) Seasonal speedup of a Greenland marine-terminating outlet glacier
853 forced by surface melt–induced changes in subglacial hydrology. *Journal of Geophysical*
854 *Research: Earth Surface* **116**(F3) (doi:10.1029/2010JF001948)
- 855 Stott J (2005) BBC R&D White Paper WHP 109: Digital Radio Mondiale: DRM, digital radio on long,
856 medium and short waves – another radio revolution?
857 <http://downloads.bbc.co.uk/rd/pubs/whp/whp-pdf-files/WHP109.pdf>
- 858 Tedstone AJ, Nienow PW, Gourmelen N, Dehecq A, Goldberg D and Hanna E (2015) Decadal
859 slowdown of a land-terminating sector of the Greenland Ice Sheet despite warming. *Nature*
860 **526**(7575), 692–695 (doi:10.1038/nature15722)
- 861 Tranter M, Sharp MJ, Lamb HR, Brown GH, Hubbard BP and Willis IC (2002) Geochemical weathering
862 at the bed of Haut Glacier d’Arolla, Switzerland—a new model. *Hydrological Processes* **16**(5),
863 959–993 (doi:10.1002/hyp.309)
- 864 UM10204 I2C-bus specification and user manual (2014) NXP Semiconductors, Eindhoven,
865 Netherlands <https://www.nxp.com/docs/en/user-guide/UM10204.pdf>
- 866 Walder JS (1986) Hydraulics of Subglacial Cavities. *Journal of Glaciology* **32**(112), 439–445
867 (doi:10.3189/S0022143000012156)
- 868 Werder MA, Schuler TV and Funk M (2010) Short term variations of tracer transit speed on alpine
869 glaciers. *The Cryosphere* **4**(3), 381–396 (doi:10.5194/tc-4-381-2010)
- 870 Young TJ and 8 others (2018) Resolving the internal and basal geometry of ice masses using imaging
871 phase-sensitive radar. *Journal of Glaciology* **64**(246), 649–660 (doi:10.1017/jog.2018.54)
- 872
- 873

874 **APPENDIX A – BATTERY LIFE CALCULATION**

875 Table A1 – battery life calculation

876

Activity	Quantity	Unit
Energy consumption during measure and transmit	0.5	J
Duration of measure and transmit	3.2	s
Current consumption during sleep	500	nA
Nominal battery voltage	3.7	V
Power consumption during sleep	1.85	uW
Battery nominal voltage	3.7	V
Battery nominal capacity	400	mAh
Battery nominal capacity	1.48	Wh
Battery nominal capacity	5328	J
Derate factor for operating in the cold	50%	
Battery effective capacity in the field	2664	J
For 2 measurements per day:		
Active measurement time per day:	6.4	seconds
Sleep time per day	86393.6	seconds
Energy used whilst active	1	J
Energy used whilst asleep	0.16	J
Total energy used per day	1.16	J
Number of days the system will run for	2296	days
Number of years the system will run for	6.3	years

877